Peng *et al. Energy Mater.* **2025**, *5*, 500060
DOI: 10.20517/energymater.2024.247

Energy Materials

Article

Open Access

Modulating electronic structure of Co-N_5S_1 sites in Co single atom catalysts via phosphorus incorporation and nanoclusters to promote oxygen electrocatalytic activity

Jing Peng[1], **Ting Xue**[1], **Zhitong Li**[1], **Junwei Shi**[1], **Xingzhu Wang**[1,2,*], **Baomin Xu**[1,*]

[1]Department of Materials Science and Engineering, and SUSTech Energy Institute for Carbon Neutrality, Southern University of Science and Technology, Shenzhen 518055, Guangdong, China.
[2]Shenzhen Putai Technology Co., Ltd, Shenzhen 518110, Guangdong, China.

[*]**Correspondence to:** Prof. Xingzhu Wang, Department of Materials Science and Engineering, and SUSTech Energy Institute for Carbon Neutrality, Southern University of Science and Technology, Taoyuan Street, Nanshan district, Shenzhen 518055, Guangdong, China. Shenzhen Putai Technology Co., Ltd, Guanlan Street, Longhua District, Shenzhen 518110, Guangdong, China. E-mail: wangxz@sustech.edu.cn; Prof. Baomin Xu, Department of Materials Science and Engineering, and SUSTech Energy Institute for Carbon Neutrality, Southern University of Science and Technology, Taoyuan Street, Nanshan District, Shenzhen, 518055, China. E-mail: xubm@sustech.edu.cn

How to cite this article: Peng, J.; Xue, T.; Li, Z.; Shi, J.; Wang, X.; Xu, B. Modulating electronic structure of Co-N_5S_1 sites in Co single atom catalysts via phosphorus incorporation and nanoclusters to promote oxygen electrocatalytic activity. *Energy Mater.* **2025**, *5*, 500060. https://dx.doi.org/10.20517/energymater.2024.247

Received: 4 Nov 2024 **First Decision:** 3 Dec 2024 **Revised:** 12 Dec 2024 **Accepted:** 17 Dec 2024 **Published:** 27 Feb 2025

Academic Editor: Wei Tang **Copy Editor:** Ping Zhang **Production Editor:** Ping Zhang

Abstract

Atomically dispersed metal catalysts coordinated with nitrogen coordination and anchored to carbon substrates (M-N-C) have become highly effective alternatives to platinum-group catalysts for oxygen electrocatalysis. However, the catalytic efficacy of M-N-C systems remains constrained by the suboptimal performance associated with the symmetric charge distribution around the active metal centers. The synergistic co-design of asymmetric metal single-atom catalytic centers with heteroatom doping significantly enhances the bifunctional oxygen electrocatalytic activity and durability, advancing the capabilities of next-generation flexible zinc-air batteries. Herein, we developed a pyrolysis-secondary coordination strategy to generate a bifunctional oxygen electrocatalyst, characterized by single Co atoms integrated within an asymmetrical Co-N_5S_1 moiety, along with nanocluster complexes embedded in N,P,S-codoped carbon frameworks, labeled Co_{SA+NC}/NPSC. In the Co_{SA+NC}/NPSC catalyst, the Co-N_5S_1 active sites exhibit an optimized electronic configuration, achieved through the synergistic coordination of heteroatom doping and nanocluster integration. Theoretically, this configuration significantly lowers the energy barriers and adjusts the d-band center, ensuring a more balanced binding strength between active sites and the oxygen-containing intermediates and contributing to the promoted bifunctional oxygen reduction reaction/oxygen evolution reaction efficiency. The experimentally analytical results reveal that the Co_{SA+NC}/NPSC demonstrates an impressive oxygen evolution reaction activity ($E_{j=10}$ = 1.58 V) and a narrow bifunctional potential gap (ΔE = 0.75 V), remarkably superior to the counterparts with symmetric Co-S coordination or phosphorus-free doping. When assembled as an air electrode, the Co_{SA+NC}/NPSC-based flexible zinc-air battery exhibits ultralong charge-discharge life (> 105 h) and impressive initial round-trip efficiency of 72.42% even at 0 °C.

Keywords: Asymmetric metal single-atom, heteroatom doping, bifunctional oxygen electrocatalyst, flexible zinc-air battery

INTRODUCTION

The development of advanced catalysts equipped with green renewable energy conversion and storage technologies, such as zinc-air batteries (ZABs), lithium-sulfur batteries, lithium-air batteries, and fuel cells, presents exciting new opportunities for harnessing sustainable energy moving forward[1,2]. For these devices, a superior bifunctional oxygen electrocatalyst is a cornerstone of the cathodes. These are indispensable to expedite the practical reaction rates in the oxygen evolution reaction (OER) and oxygen reduction reaction (ORR) process. Noble metal-based composites (such as Pt/C, Pd/C, Ru/C, Ir/C, *etc.*) with cutting-edge performance are predominantly utilized to enhance the ORR/OER process. However, due to their catalytic selectivity, sustainability, and scarcity, the further adoption of noble metal-based catalysts in the commercial market is severely constrained. This situation considerably encourages the exploration of potential substitutes. Recently, innumerable attention has been centralized on developing transition metal-based catalysts possessing practically equivalent electrocatalytic activity, excellent economic affordability, and structural robustness. Specially, single-atomic catalysts (SACs) featuring the four-coordinated MN_4 moiety (M=Fe, Mn, Ni, Co, Cu, *etc.*), with an ultrahigh atom utilization rate and tunable electronic properties, are among the most popular electrocatalytic materials in investigation[3,4]. Ji *et al.* developed a single-atom iron catalyst on two-dimensional nitrogen-doped carbon support with defects (Fe_1/DNC) using a microenvironment engineering approach[5]. Fe_1/DNC catalysts demonstrated remarkable ORR activity in an extremely wide pH range (alkaline, acidic, and neutral) because of the synergistic enhancement impact of defect-induced electrical characteristics and $FeN_4(OH)$ moieties. In addition, Co-N_4-C-[6-8] and Mn-N_4-C[9,10] -based electrocatalysts also achieved fine electrocatalytic activity in the former research. Nevertheless, in the wake of further experimental studies and theoretical calculations, the symmetric microenvironment of MN_4 in SACs may lead to suboptimal adsorption/desorption processes in electrocatalytic reactions, limiting the reaction kinetics of the catalyst[11-13].

Hitherto, introducing a second active site[14-16], nanoclusters (NCs)[17,18], and heteroatoms[19-21] in MN_4 catalysts were corroborated to the major ways to break the symmetry of the planar structure, optimizing both electrocatalytic activity and stability of metal-nitrogen-carbon (M-N-C) composites. On the one hand, plentiful studies have manifested that the import of additional active metal atoms largely enhanced the site density of the catalysts, realizing a multi-functional synergism and excellent catalysis[22,23]. For example, Li *et al.* developed a Fe-Co bimetallic monoatomic catalyst with asymmetric configurations [Fe-Co(DSA)@3DNC][24]. For the seesaw interaction of the bimetallic atom, the d-band center of Fe-Co(DSA)@3DNC kept a downward shift than the symmetric Fe-Co model, which was conducive to promoting the dissociation of oxygen intermediates and boosting the ORR/OER bifunctional activity of the catalyst. Additionally, Rao *et al.* proposed a high-entropy single-atom catalyst with several different single-atom centers dispersed on an N-doped carbon skeleton, and the quinary FeCoNiCuMn catalyst exhibited more excellent activity and durability than the benchmark Pt/C catalyst in electrochemical terms[25]. Nevertheless, the structure-activity relationship and underlying reaction mechanism in multi-site systems remain in the infancy stages of understanding, presenting considerable challenges for conquering technical bottlenecks. On the other hand, tremendous investigation efforts were devoted to analyzing the NCs or heteroatoms (S, P, B, *etc.*) doping on the M-N-C catalysts and clarifying the relationship between the microenvironment and catalytic performance[26,27]. Among these studies, phosphorus presented a distinct doping effect on M-N-C systems, promoting catalytic activity more effectively than other heteroatoms due to the stronger electron-donation ability[28,29]. Notably, phosphorus doping favors enhancing electro-oxidation resistance while mitigating carbon corrosion throughout electrocatalytic processes. Zhou *et al.* have successfully incorporated phosphorus atoms into the Fe-N-C to construct the second coordination, and the P/Fe-N-C catalyst demonstrated extraordinarily bifunctional catalytic activity with an exceptionally narrow potential gap ($\triangle E = 0.63$ V), outperforming the Fe-N-C counterpart[30]. Furthermore, extensive experimental investigation and density functional theory (DFT) calculations revealed that metal NCs can act as effective promoters for M-N-C system catalysts, significantly enhancing their catalytic efficiency toward the ORR[31,32]. The interaction between the M atom in the M-N_4 structure and the surrounding NCs induced a downward shift in the d-band center, which weakened the binding affinity for *OH intermediates and optimized the catalytic efficiency for ORR by facilitating faster intermediate dissociation and electron transfer[33]. Hence, the controlled anchoring of NCs and the implementation of asymmetric hetero-atomic coordination onto a porous carbon framework represent an encouraging strategy forging significant improvements in the electrocatalytic efficiency and stability of M-N-C catalysts for oxygen reactions.

Toward that end, through a straightforward pyrolysis-secondary coordination process using amberlite@Co^{2+} as the precursor, we designed a catalyst with cobalt NCs-decorated asymmetric CoN_5S_1 single-atom sites anchored in N, S, and P-codoped carbon nanosheets, labeled Co_{SA+NC}/NPSC. The nitrogen-rich melamine (MA) was introduced *in situ* into the amberlite@Co^{2+} precursor, where nitrogen invaders partially substituted for the original Co-S moiety, prompting the generation of asymmetric Co-N_5S_1 sites. Simultaneously, triphenylphosphine was utilized as a phosphorus source to modulate the electron configuration of the Co SA active centers, thereby elevating the electrocatalytic efficiency and stability of the Co_{SA+NC}/NPSC catalyst. Notably, by virtue of the distinct atomic structural configuration, the optimized Co_{SA+NC}/NPSC delivered markedly improved activities toward OER ($E_{j=10}$ = 1.58 V) and a narrow bifunctional potential gap ($\Delta E = 0.753$ V), which was superior to the counterparts featuring symmetrical Co-S coordination or phosphorus-free doping. According to the theoretical simulation of the ORR and OER processes, the Co_{SA+NC}/NPSC catalyst demonstrated the lowest energy barrier, which is unified with the accelerated reaction kinetics in the experiment. When integrated into an air electrode, the Co_{SA+NC}/NPSC catalyst-based flexible ZAB demonstrated exceptional charge-discharge cycle stability (over 105 h) and impressive initial round-trip efficiency of 72.42% at 0 °C and 5 mA cm^{-2}.

EXPERIMENTAL

Chemicals and reagents

Amberlite 732 [$(C_{10}H_{10}C_8H_8O_3SNa)_x$, analytical reagent (AR), Aladdin], cobalt chloride hexahydrate ($CoCl_26H_2O$, AR, Aladdin), sodium hydroxide (NaOH, AR, Aladdin), hydrochloric acid (HCl, AR, Aladdin), polymethyl methacrylate (PMMA) powder {$-[CH_2C(CH_3)(COOCH_3)]_n-$, AR, Sigma-Aldrich}, triphenylphosphine ($C_{18}H_{15}P$, AR, TCI Shanghai), MA ($C_3H_6N_6$, AR, McLean), anhydrous ethanol (C_2H_6O, AR, Aladdin), platinum carbon composite (Pt/C, 20 wt%, Johnson Matthey), iridium oxide (IrO_2, 86%, Suzhou Sinero Technology), acrylamide (C_3H_5NO, AR, Aladdin), N, N'-methylenebisacrylamide ($C_7H_{10}N_2O_2$, AR, Aladdin), potassium persulfate ($K_2S_2O_8$, AR, Aladdin), potassium hydroxide (KOH, 95%, Aladdin), zinc acetate dihydrate ($C_4H_{10}O_6Zn$, 99%, Aladdin), zinc foil (0.5 mm, 99.9%, Sike) and carbon cloth (W1S1011, Suzhou Sheng'erno Technology) were directly used as received.

Catalysts synthesis

Preprocessing of amberlite 732

The pretreatment of amberlite 732 was performed sequentially using deionized water, sodium hydroxide, and hydrochloric acid. Initially, an excess of Milli-Q water was added to amberlite 732. The mixture was stirred for 24 h to thoroughly rinse the resin, with repeated replacements of Milli-Q water. Subsequently, dilute hydrochloric acid (5 wt%) and sodium hydroxide (5 wt%) solutions were sequentially input to remove residual impurities and facilitate ion exchange between hydrogen and sodium ions. After the pretreatment, amberlite 732 was reclaimed by filtration and dried at 50 °C.

Preparation of amberlite@Co^{2+} precursor

First, 1.0 g of dried amberlite 732 and 200 mL of 0.1 M cobalt (II) chloride hexahydrate solution were combined in a beaker and allowed to react for 24 h to facilitate cobalt ion exchange. The resulting amberlite@Co^{2+} precursor was isolated by suction filtration and thoroughly rinsed with Milli-Q water. After drying, the amberlite@Co^{2+} precursor was ground into powder using ball milling, followed by sieving to obtain fine particles. A 1.0 g portion of amberlite@Co^{2+} powder was ultrasonically redispersed in 30 mL of anhydrous ethanol, to which PMMA was added in a mass ratio of 0.5:1 (amberlite@Co^{2+}), along with 150 mg of triphenylphosphine (PPh$_3$). The even dispersion was imported into a 100 mL round-bottom flask. The homogeneous mixture was collected via rotary evaporation at 50 °C under vacuum, yielding the product amberlite@Co^{2+}/PMMA/PPh$_3$. During the preparation, PMMA was designated as the soft template, with PPh$_3$ supplying the phosphorus source.

Preparation of Co$_{SA+NC}$/NPSC

The amberlite@Co^{2+}/PMMA/PPh$_3$ precursor was thoroughly ground with adequate MA powder before being transferred to a tube furnace. In the initial heating phase, the temperature was controlled to 600 °C at a constant heating rate (2.5 °C min^{-1}) and maintained for 2 h. Subsequently, the temperature was elevated to 900 °C for an additional 2 h under Ar atmosphere, and the obtained product was labeled Co$_{SA+NP}$/NPSC. After calcination, the resulting Co$_{SA+NP}$/NPSC material was further treated with a 0.3 M hydrochloric acid solution to dissolve any metal nanoparticles agglomerated during pyrolysis. The generated precipitate was collected via filtration and dried using freeze-drying, yielding the final product, designated as Co$_{SA+NC}$/NPSC.

Preparation of Co$_{SA+NC}$/SC and Co$_{SA+NC}$/NSC

To investigate the influence of varying coordination environments and heteroatom doping on catalytic performance, Co$_{SA+NC}$/SC and Co$_{SA+NC}$/NSC catalysts were synthesized separately. The Co$_{SA+NC}$/SC catalyst was prepared following a protocol similar to that of Co$_{SA+NC}$/NPSC, differing only in inpouring excessive MA powder to the amberlite@Co^{2+} -PMMA precursor before calcination. In contrast, the Co$_{SA+NC}$/NSC catalyst synthesis omitted inpouring an additional phosphorus source in the precursor.

Physical characterizations

The X-ray diffraction (XRD) patterns of the catalysts were obtained using a Rigaku Smartlab 3KW X-ray diffractometer with Cu-Kα radiation. The overall morphology and elemental distribution were confirmed using a HITACHI UHR SU8230 scanning electron microscope (SEM) integrated with an energy-dispersive spectrometer (EDS). More refined details (e.g., the distribution of the NCs, corresponding diffraction, and lattice fringes) of the microscopic morphology of the catalysts were monitored by a transmission electron microscope (TEM, Tecnai G2 F20 S-Twin) in the operation voltage of 200 kV. The aperture distribution and specific surface area were calculated by N$_2$ isothermal adsorption/desorption curves, which were gathered by a 3 Flex 4.02 gas analyzer (Micrometrics). Prior to the adsorption tests, the catalysts were degassed for 10 h at 200 °C while under vacuum. An Agilent 5110 inductively coupled plasma-atomic emission spectrometer (ICP-AES) was applied to calculate the specific content of Co atoms in the samples.

The detailed coordination environment of active Co atoms within the catalysts was analyzed using X-ray absorption spectroscopy at the Shanghai Synchrotron Radiation Facility (BL14W Beamline) with Si (111) crystal monochromators. The catalysts were put into aluminum containers and then sealed with Kapton tape film prior to beamline examination. In the transmission mode, Co K-edge X-ray absorption near edge structure (XANES) spectra in the catalyst and all reference samples were captured, the same as the extended X-ray absorption fine structure (EXAFS) spectrogram. The Athena and Artemis software codes processed and analyzed the spectra. Minimal alterations of the Co K-edge XANES spectra were noted between the two scans conducted on a particular sample.

Electrochemical measurements

A CHI 760e electrochemical workstation, equipped with a PINE rotating disk electrode (RDE), was employed to manage a three-electrode system for electrochemical characterization. The Hg/HgO (1.0 M KOH) electrode functioned as the reference electrode and was calibrated in hydrogen-saturated 0.1 M or 1.0 M KOH prior to all electrochemical measurements. The thermodynamic potential was determined by recording the average potential corresponding to the zero-crossing current in a cyclic voltammogram (CV) at 5 mV s^{-1}. A glassy carbon RDE (0.196 cm^2) with uniformly dispersed catalyst slurry was assigned as the working electrode. A graphite rod was appointed as the counter electrode. The slurry of the working electrode was configured by sonicating the solution with catalyst (2 mg), anhydrous ethanol, and water (V:V = 1:1, 380 μL), along with Nafion (5 wt%, 20 μL) for 2 h. Subsequently, 20 μL of the ink was deposited onto a rotating ring-disk electrode (RRDE), yielding a catalyst loading of 0.509 mg cm^{-2}. The ink for commercial 20% Pt/C and IrO_2 catalysts was prepared in identical proportions, with the same catalyst loading of 0.509 mg cm^{-2}.

Assembly and testing of flexible zinc air batteries

The self-assembled flexible ZAB was configured in a sandwich architecture, comprising an anode (polished zinc foil), electrolyte [polyacrylamide (PAM) organohydrogel imbued with 6 M KOH and 0.2 M $Zn(Ac)_2{\cdot}2H_2O$], and a cathode catalyst (e.g., Co_{SA+NC}/NPSC, Co_{SA+NC}/SC, and Co_{SA+NC}/NSC). The air cathode consisted of a layer for the current collection made of carbon cloth, along with a film containing the catalyst. The PAM organogel electrolyte was synthesized via free radical polymerization, following the detailed procedure described herein. Specifically, a moderate amount of crosslinker (N,N'-methylenebisacrylamide), acrylamide monomer, and initiator ($K_2S_2O_8$) were sequentially dissolved in the solvent mixture of dimethyl sulfoxide (DMSO) and Milli-Q water. The initiator facilitated the formation of free radicals to drive the polymerization process. This resulting solution was imported into a transparent glass mold, sealed, and reacted at 60 °C for 13 h. Prior to use, the freshly synthesized PAM hydrogel was immersed for 72 h in an electrolyte solution containing 6 M KOH and 0.2 M $Zn(Ac)_2{\cdot}6H_2O$. To prepare the Co_{SA+NC}/NPSC catalyst ink, the mixture of Super P and catalysts (1:9) was poured in 2 mL of ethanol solution. Subsequently, 80 μL of a 5 wt% polytetrafluoroethylene (PTFE) emulsion was introduced into the ink. Following an additional hour of grinding, the excess ethanol was evaporated at room temperature, and the catalyst layer was shaped into a film and cut into 1 cm^2 squares. The catalyst layer and conductive carbon cloth were then laminated using a roller press and maintained under vacuum conditions until further use. For comparison, a commercial Pt/C+IrO_2 catalyst layer was prepared by uniformly blending 20 mg of 20% Pt/C, 20 mg of IrO_2, 80 μL of 5 wt% PTFE aqueous solution, and 2 mL of anhydrous ethanol. The loading amount of all catalysts in the air electrode is nearly 5 mg cm^{-2}. The operational performance of the flexible ZABs, particularly those based on Co_{SA+NC}/NPSC, was assessed using a Neware testing instrument under constant current densities (e.g., 2 mA cm^{-2} and 5 mA cm^{-2}), to evaluate their stability at low temperatures.

Computational methods

Theoretical calculations were carried out using DFT, as incorporated in the Vienna Ab initio Simulation Package[34]. The Perdew-Burke-Ernzerhof[35] in conjunction with the projector augmented wave method[36] was employed to ameliorate the atomic models. All atomic coordinates were relaxed during geometric optimization until the calculated forces were reduced to below 0.05 eV $Å^{-1}$. The kinetic energy cutoff was controlled at 400 eV by employing the plane wave basis set. Periodic boundary conditions were applied to the simulation of unit cells, incorporating a 15 Å vacuum layer to ensure isolation. Furthermore, the Brillouin zones were sampled using a Monkhorst-Pack grid, configured as (1 × 1 × 1)[37]. The calculations of free energy (ΔG) for each elementary step were referenced to the standard hydrogen electrode and expressed by:

$$\Delta G = \Delta E + \Delta E_{ZPE} - T\Delta S - neU \tag{1}$$

Where ΔE represents the total energy change, whereas ΔS and ΔE_{ZPE} refer to the alterations in entropy and zero-point energy, respectively. The variable n represents the number of electrons. The ORR and OER adsorption energy (ΔE_{*OH}) was further determined by:

$$\Delta E_{*OH} = E_{sbustrate + *OH} - E_{substrate} - E_{*OH} \tag{2}$$

The four intermediate steps in the ORR and OER process are enumerated as follows:

$$* + O_2 + H^+ + e^- \rightarrow *OOH \tag{3}$$

$$*OOH + H^+ + e^- \rightarrow *O + H_2O \tag{4}$$

$$*O + H^+ + e^- \rightarrow *OH \tag{5}$$

$$*OH + H^+ + e^- \rightarrow H_2O + * \tag{6}$$

The d-band center (ε_d) is assessed by applying[38]:

$$\varepsilon_d = \frac{\int_{-\infty}^{+\infty} \varepsilon\rho(\varepsilon)d\varepsilon}{\int_{-\infty}^{+\infty} \varepsilon d\varepsilon} \tag{7}$$

Where $\rho(\varepsilon)$ denotes the density of states, and ε represents the energy eigenvalue.

RESULTS AND DISCUSSION

The synthesis of a nitrogen, sulfur, and phosphorus co-doped nanocarbon catalyst, featuring abundant isolated cobalt single-atom active sites and cobalt NCs, facilitated by an excess nitrogen-source-assisted pyrolysis strategy (MA), was depicted in Figure 1A. Initially, Co^{2+} ions were firmly encapsulated within the amberlite 732 resin through ion exchange, yielding an amberlite@Co^{2+} hybrid structure. Subsequently, the amberlite@Co^{2+} precursor was thoroughly mixed with PMMA, PPh_3, and ethanol solution to incorporate soft templates and phosphorus sources. The resulting amberlite@Co^{2+}/PMMA/PPh_3 composite was then uniformly ground with MA to achieve a homogeneous mixture. This mixture was subjected to thermal treatment in a corundum crucible at 900 °C for 2 h under an argon atmosphere. During the pyrolysis, as the temperature approached the decomposition points of PMMA (270 °C) and MA (300 °C), the polymers decomposed, releasing gaseous products and forming layered C_3N_4, thereby generating a porous substrate.

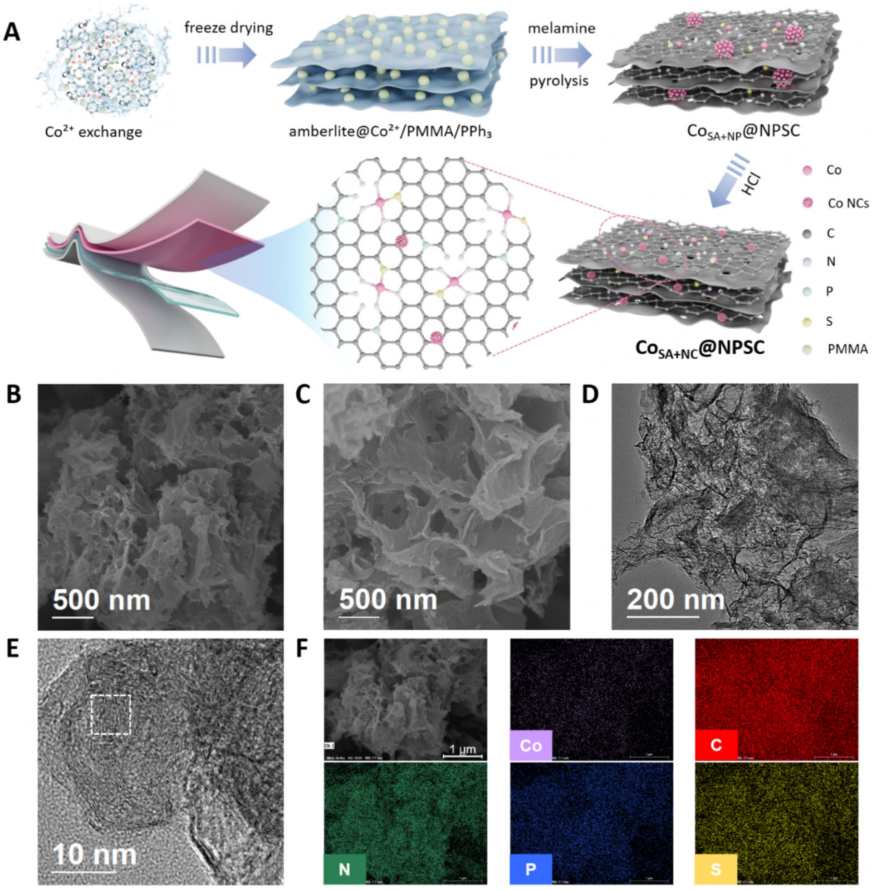

Figure 1. (A) The synthesis flowchart of Co_{SA+NC}/NPSC; SEM pictures of (B) Co_{SA+NP}/NPSC and (C) Co_{SA+NC}/NPSC; (D) TEM image; (E) HRTEM image; and (F) EDS mapping of Co_{SA+NC}/NPSC. SEM: Scanning electron microscope; TEM: transmission electron microscope; HRTEM: high resolution transmission electron microscopy; EDS: energy-dispersive spectrometer.

At higher temperatures (> 500 °C), the amberlite@Co^{2+}/PMMA/PPh_3 composite underwent carbonization, generating two-dimensional graphene-like nanosheets enriched with nitrogen, phosphorus, sulfur, and cobalt species. As shown in Figure 1B, the Co_{SA+NP}/NPSC catalyst featured aggregated nanocrystals dispersed across the carbon matrix. Notably, MA served as an efficient nitrogen source, facilitating the formation of Co-N coordination within the carbon nanosheets, disrupting the symmetric Co-S coordination environment, and leading to the formation of asymmetric CoN_5S_1 sites. Following the annealing process, the final Co_{SA+NC}/NPSC electrocatalyst was obtained by treating the product with dilute hydrochloric acid (0.3 M) to remove any residual metallic nanoparticles. To elucidate the synergistic effects of the coordination environment and heteroatom doping on the active sites, control samples without phosphorus doping (Co_{SA+NC}/NSC) and with symmetric S coordination (Co_{SA+NC}/SC) were also synthesized for comparative analysis. As illustrated in Supplementary Figure 1, the Co_{SA+NC}/NSC exhibited a well-defined two-dimensional nanosheet structure, suggesting a higher surface area contrasted to the stacked morphology of Co_{SA+NC}/SC. The morphological characteristics of the catalysts were initially investigated through SEM [Figure 1C] and TEM. As illustrated in Figure 1D, the TEM image of the synthesized Co_{SA+NC}/NPSC catalyst revealed a two-dimensional nanosheet structure with thin layers, devoid of any discernible metal nanoparticles. Further structural details of Co_{SA+NC}/NPSC were obtained via high resolution transmission electron microscopy (HRTEM) [Figure 1E]. Supplementary Figure 2A displayed the enlarged details in the circled area of Figure 1E, which showed distinct lattice fringes with interplanar spacings of 0.33 nm, indicative of the presence of cobalt NCs anchored within the carbon nanosheet, corresponding to the (111) plane of these NCs [Supplementary Figure 2B]. Furthermore, Co_{SA+NC}/NPSC exhibited no evident diffraction bright spots attributable to cobalt NCs, aligning with the ring-like selected area electron diffraction (SAED) patterns shown in Supplementary Figure 2C, indicating the existence of only a handful of cobalt NCs. EDS mapping in Figure 1F confirmed the homogeneous distribution of Co, C, N, S, and P across the entire Co_{SA+NC}/NPSC catalyst. ICP-AES analysis data was listed in Supplementary Table 1, which further presented that the actual content of Co atoms in Co_{SA+NC}/NPSC was approximately 1.64 wt%. XRD curves were characterized to record the transformation of the crystallization state from Co_{SA+NP}/NPSC to Co_{SA+NC}/NPSC. As represented in Supplementary Figure 3A, the XRD pattern of Co_{SA+NP}/NPSC demonstrated diffraction peaks at 44.8°, 51.6°, and 76.0°, which correspond to the different planes of Co nanoparticles (JCPDS No.15-0806). Following acid treatment, the diffraction peaks are attributed to the Co crystal planes disappear entirely, while the two broad peaks observed at 25.4° and 43.8° correspond to the different planes of graphitic carbon (JCPDS No.41-1487), respectively, consistent with the SEM and TEM results [Supplementary Figure 3B]. Similarly, the XRD patterns of Co_{SA+NP}/NSC [Supplementary Figure 3C] and Co_{SA+NP}/SC [Supplementary Figure 3D] also confirm the existence of graphitic carbon substracts, with no other impurities detected. To further elucidate the pore structure of the catalysts, nitrogen adsorption-desorption isotherms were recorded. The isotherms for Co_{SA+NC}/NPSC, Co_{SA+NC}/NSC, and Co_{SA+NC}/SC, shown in Supplementary Figure 4A-C, demonstrated typical type IV isotherms, indicating the presence of a substantial number of mesopores and micropores. A comparison of the Brunauer-Emmett Teller (BET) surface areas revealed that importing the nitrogen source significantly enhanced the surface area of Co_{SA+NC}/NSC relative to Co_{SA+NC}/SC, facilitating the dispersion of more active sites [Supplementary Figure 4D-F].

XANES and EXAFS spectroscopy were favorable descriptors to elucidate the detailed layout and chemical state of the Co atom active centers comprehensively. As shown in Figure 2A, the near-edge absorption energy of Co_{SA+NC}/NPSC was situated near that of CoO, indicating the presence of a positively charged Co species, primarily in the Co^{2+} oxidation state. The coexistence of metallic Co-Co, Co-N, and Co-S scattering pathways suggested the coordinating atoms around the Co atom are N, S and Co atoms, respectively [Figure 2B]. To further explore the coordination environment, wavelet transform (WT)-EXAFS analysis was employed, offering enhanced resolution by distinguishing backscattering atoms, even in cases of substantial overlap in R-space, while simultaneously providing both radial distance and k-space resolution. Figure 2C presents the WT contour plots for the three k^2-weighted $\chi(k)$ signals, derived using Morlet wavelets for optimal resolution. The intensity maxima, corresponding to distinct coordinates (k, R), were primarily related to the path length R and the atomic number Z. Notably, Co foil and CoS_2 exhibited intensity maxima at 7.3 $Å^{-1}$ (Co-Co contribution) and 5.8 $Å^{-1}$ (Co-S contribution), respectively. For Co_{SA+NC}/NPSC, the WT analysis of the Co K-edge EXAFS predominantly showed an intensity maximum arising from Co-N scattering at lower k-space (3.8 $Å^{-1}$). Additionally, a substantial overlap was noted among the Co-N, Co-S, and Co-Co regions, indicating that these coordination environments converge within a unified region in the wavelet maps. The bond lengths and coordination numbers of the catalyst were calculated by least-squares EXAFS fitting analysis. The K-space and R-space fitting curves indicated a strong correlation with the experimental spectra [Figure 2D-G, Supplementary Figure 5, and Supplementary Table 2]. Based on these results, the coordination around the central Co atom revealed an average coordination number of six, comprising five nitrogen atoms and one sulfur atom. As summarized in Supplementary Table 2, the EXAFS fitting parameters for the Co-Co and Co-S pathways in Co_{SA+NC}/NPSC indicated bond lengths of 2.46 Å and 2.32 Å, respectively, which were marginally shorter than those observed for Co foil (2.49 Å) and CoS_2 (2.31 Å). These findings collectively affirmed that the Co_{SA+NC}/NPSC catalyst predominantly comprises CoN_5S_1 moieties, accompanied by a trace amount of cobalt NCs.

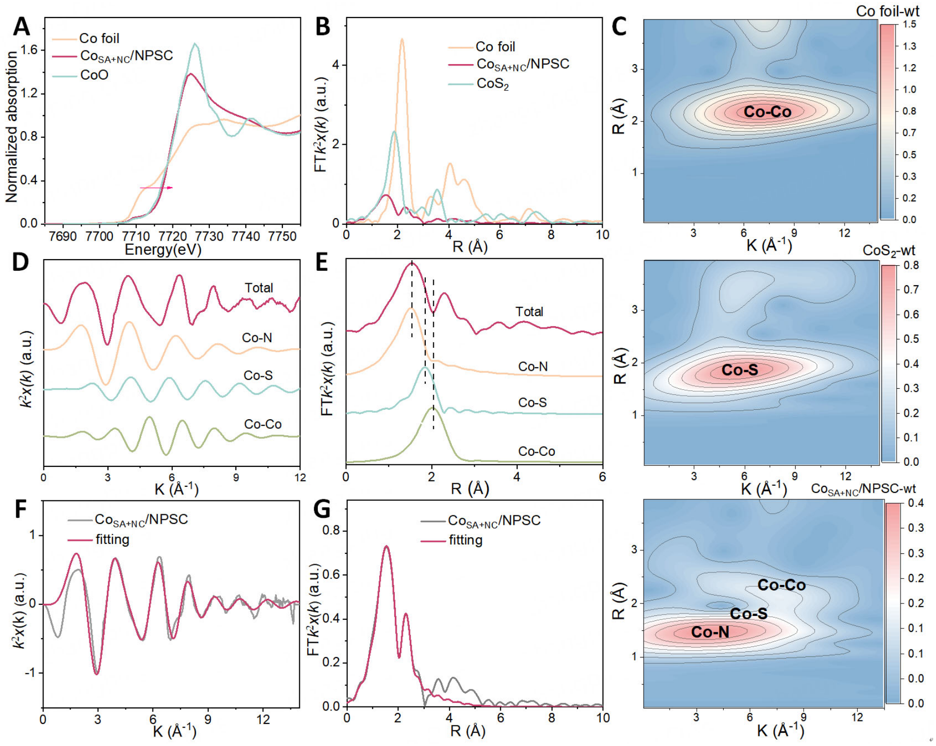

Figure 2. (A) XANES spectra for the Co foil, CoO and Co$_{SA+NC}$/NPSC; (B) FT-EXAFS spectra of Co K-edge in Co$_{SA+NC}$/NPSC; (C) k^2-weighted WT-EXAFS signals of Co foil, CoS$_2$ and Co$_{SA+NC}$/NPSC; EXAFS analysis of Co$_{SA+NC}$/NPSC at (D) k and (E) R spaces, respectively; Fitting results of Co K-edge FT-EXAFS analysis in (F) k and (G) R spaces for Co$_{SA+NC}$/NPSC. XANES: X-ray absorption near edge structure; EXAFS: extended X-ray absorption fine structure; FT-EXAFS: fourier transform- extended X-ray absorption fine structure; WT-EXAFS: wavelet transform- extended X-ray absorption fine structure.

The ORR activity of the Co$_{SA+NC}$/NPSC catalyst was rigorously evaluated using a RDE in 0.1 M KOH solution, with the Co$_{SA+NC}$/NSC and Co$_{SA+NC}$/SC catalysts used for comparative analysis. As illustrated in Figure 3A, the linear sweep voltammetry (LSV) curves confirmed that the Co$_{SA+NC}$/NPSC catalyst exhibited superior ORR performance relative to its Co$_{SA+NC}$/NSC and Co$_{SA+NC}$/SC counterparts, as evidenced by a significantly reduced overpotential. Notably, the half-wave potential ($E_{1/2}$) of Co$_{SA+NC}$/NPSC was measured at 0.827 V, markedly outperforming that of Co$_{SA+NC}$/NSC (0.803 V) and Co$_{SA+NC}$/SC (0.695 V). The ORR kinetics were further examined by evaluating the Tafel slope, as depicted in Figure 3B. The Co$_{SA+NC}$/NPSC catalyst exhibited a Tafel slope of 45.7 mV dec^{-1}, lower than those of Co$_{SA+NC}$/NSC (50.5 mV dec^{-1}) and Co$_{SA+NC}$/SC (89.1 mV dec^{-1}), signifying faster ORR kinetics for Co$_{SA+NC}$/NPSC. Beyond its competitive catalytic activity, the catalyst favored a highly selective four-electron (4e$^-$) ORR pathway, a crucial factor for minimizing the generation of deleterious H_2O_2 byproducts, which could otherwise undermine catalyst stability. The catalytic selectivity was evaluated via Koutecky-Levich (K-L) plots [Supplementary Figure 6], with the K-L curves for Co$_{SA+NC}$/NPSC across a range of rotation speeds (400-2025 rpm) confirming a predominant 4e$^-$ ORR pathway (n = 4.03), which was superior to its counterparts. The enhanced selectivity likely stems from stronger Co-O interactions in Co$_{SA+NC}$/NPSC, facilitating efficient O-O bond cleavage along the 4e$^-$ ORR route. This exceptional selectivity also contributed to the catalyst's promising long-term stability, as demonstrated by the chronoamperometric response of Co$_{SA+NC}$/NPSC at 0.7 V versus reversible hydrogen electrode, where it retained 90.81% of its initial current after 24,000 s of continuous operation, affirming robust electrochemical stability in alkaline media [Figure 3C]. The OER efficacy of the Co$_{SA+NC}$/NPSC catalyst was assessed in 1.0 M KOH to evaluate its bifunctional catalytic performance in advanced ZABs. As shown in Figure 3D and E, the LSV curve of Co$_{SA+NC}$/NPSC exhibited the lowest

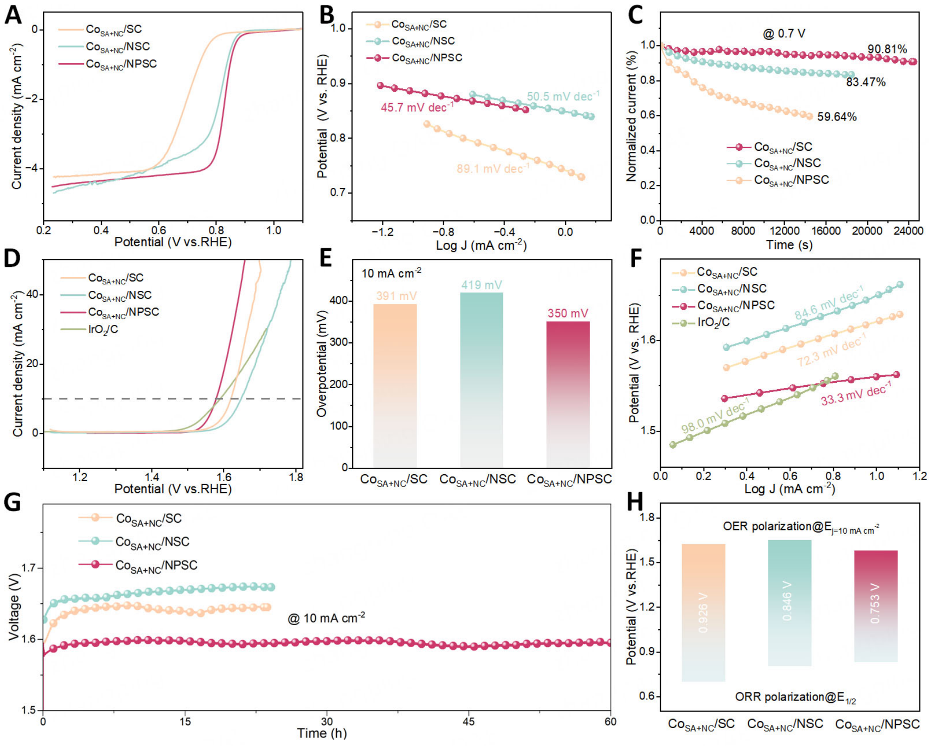

Figure 3. (A) ORR curves and (B) derived Tafel slopes Co$_{SA+NC}$/SC, Co$_{SA+NC}$/NSC and Co$_{SA+NC}$/NPSC; (C) Chronoamperometric response of Co$_{SA+NC}$/SC, Co$_{SA+NC}$/NSC and Co$_{SA+NC}$/NPSC catalyst at 0.7 V; (D) OER polarization curves; (E) overpotential and (F) the corresponding Tafel slopes of Co$_{SA+NC}$/SC, Co$_{SA+NC}$/NSC, and Co$_{SA+NC}$/NPSC catalysts; (G) The chronopotentiometry curves of Co$_{SA+NC}$/SC, Co$_{SA+NC}$/NSC, and Co$_{SA+NC}$/NPSC were taken at 10 mA cm^{-2}; (H) The potential gap ($\Delta E = E_{j=10} - E_{1/2}$) of different catalysts. ORR: Oxygen reduction reaction; OER: oxygen evolution reaction.

overpotential of 350 mV at a current density of 10 mA cm^{-2}, presenting a notable negative shift compared to Co$_{SA+NC}$/NSC (41 mV), Co$_{SA+NC}$/SC (69 mV) and the IrO$_2$/C benchmark (11 mV). The Co$_{SA+NC}$/NPSC catalyst further demonstrated superior OER kinetics, as reflected by the lowest Tafel slope of 33.3 mV dec^{-1}, in contrast to 82.6, 72.3, and 98.0 mV dec^{-1} for Co$_{SA+NC}$/NSC, Co$_{SA+NC}$/SC and IrO$_2$/C, respectively [Figure 3F]. This substantial enhancement in OER activity was likely due to the improved interaction with reaction intermediates, as theoretical studies suggested that the OER performance of Co$_{SA+NC}$/NSC and Co$_{SA+NC}$/SC was limited by weaker intermediate binding. Furthermore, the durability of Co$_{SA+NC}$/NPSC in OER electrocatalysis was confirmed by its stable chronopotentiometric response, with no discernible degradation after 60 h of continuous polarization at 10 mA cm^{-2} [Figure 3G]. In comparison, the potentials for Co$_{SA+NC}$/NSC and Co$_{SA+NC}$/SC increased to 1.673 V and 1.645 V, respectively, after 24 h under the same conditions. The bifunctional catalytic activity was quantified using the potential difference (ΔE) between the $E_{1/2}$ and the OER potential ($E_{j=10}$), where a smaller ΔE indicated superior bifunctional performance. The Co$_{SA+NC}$/NPSC catalyst exhibited the smallest ΔE of 0.753 V, surpassing the other catalysts [Figure 3H]. These results conclusively demonstrated that the synergistic effects of phosphorus doping and asymmetric atomic coordination in Co$_{SA+NC}$/NPSC significantly enhanced both ORR and OER activities. Furthermore, the electrochemically active surface area (ECSA), a critical indicator of intrinsic electrocatalytic activity, was assessed by measuring the electric double-layer capacitance (C_{dl}) in the non-Faradaic region, where C_{dl} was proportional to ECSA. As shown in Supplementary Figure 7, Co$_{SA+NC}$/NPSC displayed the highest C_{dl} value of 20.08 mF cm^{-2}, suggesting that the catalyst exposed more active sites, thus reinforcing its remarkable electrocatalytic ORR activity.

Given the enhanced bidirectional catalytic performance of the Co_{SA+NC}/NPSC catalyst, a flexible ZAB integrated with Co_{SA+NC}/NPSC (cathode), Zn foil (anode), and a PAM-based organic hydrogel electrolyte with exceptional low-temperature adaptability was fabricated (denoted as ZAB-Co_{SA+NC}/NPSC). Prior to assembly, the anti-freezing electrolyte was immersed in a solution of 6.0 M KOH and 0.2 M $Zn(OAc)_2$ for 48 h. Comparative ZABs were also constructed by substituting Co_{SA+NC}/NPSC with Co_{SA+NC}/NSC and Co_{SA+NC}/SC, referred to as ZAB-Co_{SA+NC}/NSC and ZAB-Co_{SA+NC}/SC, respectively. The electrochemical performance of these ZABs was first evaluated at ambient temperature. As shown in Figure 4A, ZAB-Co_{SA+NC}/NPSC exhibited a relatively high open-circuit voltage (OCV) of 1.40 V, approaching the theoretical OCV of 1.65 V for ZABs, thereby surpassing the other counterparts. Moreover, as depicted in Figure 4B, the maximum power density of ZAB-Co_{SA+NC}/NPSC reached 62.18 mW cm^{-2}, significantly outperforming ZAB-Co_{SA+NC}/NSC (33.87 mW cm^{-2}) and Co_{SA+NC}/SC (38.85 mW cm^{-2}). Figure 4C revealed that ZAB-Co_{SA+NC}/NPSC also delivered an excellent discharge plateau of 1.23 V and a specific capacity of 793.91 mAh g^{-1} at 5 mA cm^{-2}, corresponding to 96.82% of the theoretical discharge capacity of ZABs. More practically, the combination of superior bifunctional catalytic activity and an anti-freeze hydrogel electrolyte endowed the flexible ZAB with remarkable adaptability at sub-zero temperatures. Following an initial activation process and a 2 h exposure to a low-temperature chamber, ZAB-Co_{SA+NC}/NPSC demonstrated extended charge-discharge cycling (over 105 h) with a narrow charge-discharge potential gap ($\xi = 0.78$ V) at 0 °C and 5 mA cm^{-2}, outperforming the comparative ZABs [Figure 4D]. Detailed charge-discharge curves at various time intervals were magnified in Figure 4E-G. Notably, the Co_{SA+NC}/NPSC-based ZAB, owing to its superior OER and ORR catalytic activities, exhibited an initial round-trip efficiency (ε) of 72.42% and a charge-discharge potential gap of 0.475 V in region I, far surpassing ZAB-Co_{SA+NC}/NSC ($\varepsilon = 67.98\%$, $\xi = 0.564$ V) and ZAB-Co_{SA+NC}/SC ($\varepsilon = 59.80\%$, $\xi = 0.788$ V) [Figure 4E]. Impressively, ZAB-Co_{SA+NC}/NPSC maintained a high efficiency of 66.8% after 30 cycles, with only a slight increase in the voltage gap of 117 mV. In contrast, the round-trip efficiency of ZAB-Co_{SA+NC}/NSC declined significantly to 49.21% after 30 cycles at 5 mA cm^{-2} and 0 °C, highlighting its inferior low-temperature tolerance and structural stability [Figure 4F]. Furthermore, in region III, the Co_{SA+NC}/NPSC-based ZAB retained its advantage with an efficiency of 64.1% and a potential gap of 0.656 V, while the potential gap of ZAB-Co_{SA+NC}/SC increased to 1.474 V, more than twice that of ZAB- Co_{SA+NC}/NPSC [Figure 4G]. The discharge curves with a distinct step-like shape, shown in Figure 4H, indicated that ZAB-Co_{SA+NC}/NPSC provided the highest discharge plateaus among the comparative ZABs across various current densities, especially at higher current densities, underscoring its potential for practical applications. To further investigate the underlying kinetic processes, electrochemical impedance spectroscopy (EIS) was employed to evaluate the interfacial resistance (R_s) and charge transfer resistance (R_{ct}) of ZAB-Co_{SA+NC}/NPSC. The frequency range was controlled between 100 kHz and 1 Hz, with the ZABs in an open-circuit state throughout the experiment. As presented in Supplementary Figure 8A, the EIS fitting curves indicated that ZAB-Co_{SA+NC}/NPSC exhibited the lowest R_s and R_{ct} values, correlating with excellent rechargeability. Conversely, the increased internal resistance in ZAB-Co_{SA+NC}/NSC and ZAB-Co_{SA+NC}/SC resulted in greater ohmic polarization and reduced ion conductivity, thereby compromising their overall battery performance. To gain deeper insights into the structure-activity relationship, the microstructure of the Co_{SA+NC}/NPSC electrode was examined via TEM after several charge-discharge cycles. Supplementary Figure 8B demonstrated that Co_{SA+NC}/NPSC retained its original nanosheet morphology even after repeated cycling, consistent with the experimental data shown in Figure 4D and H. In conclusion, the exceptional rechargeability and low-temperature reversibility of Co_{SA+NC}/NPSC can be attributed to two key factors. First, its unique microstructure facilitated the full exposure of abundant active sites, significantly reducing ion diffusion distances and minimizing interfacial impedance, thereby mitigating the negative effects of sluggish ion diffusion kinetics at low temperatures. Second, the synergistic effects of asymmetric Co single-atom active sites, cobalt NCs, and heteroatom doping in Co_{SA+NC}/NPSC reduced the activation energy barrier for oxygen electrocatalysis, allowing the catalyst to maintain superior performance under low-temperature conditions.

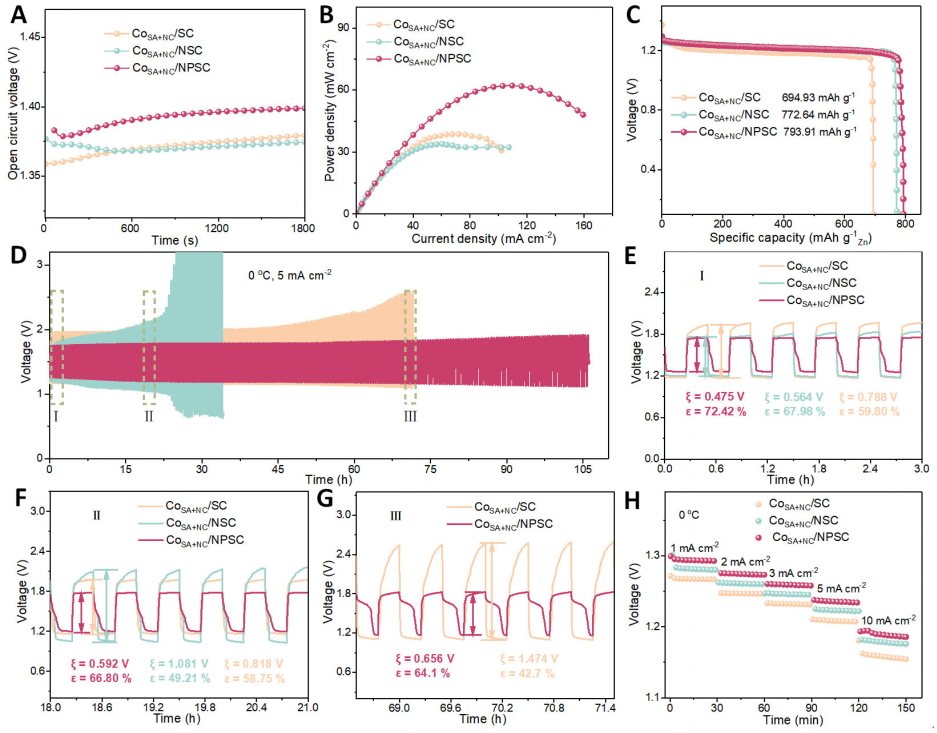

Figure 4. (A) Open-circuit voltage; (B) discharge power density plots and (C) the discharge specific capacity curves of flexible ZABs with Co_{SA+NC}/SC, Co_{SA+NC}/NSC and Co_{SA+NC}/NPSC cathode catalysts; (D) Cycling stability of the flexible ZABs at 0 °C and 5 mA cm^{-2}); The enlarged (E) region I, (F) region II and (G) region III of (D); (H) discharge curves of Co_{SA+NC}/SC, Co_{SA+NC}/NSC and Co_{SA+NC}/NPSC-based apparatus at different current densities. ZABs: Zinc-air batteries.

To elucidate the synergistic effects of heteroatom doping and cobalt NCs on the properties of asymmetric CoN_5S_1 sites, and their promoted bifunctional oxygen electrocatalytic activity, DFT calculations were performed. Based on the findings from X-ray absorption fine structure analysis, four potential structural models of Co_{SA+NC}/NPSC are illustrated in Supplementary Figure 9. The optimized atomic configuration was identified according to the criteria of minimal formation energy and a stable oxygen intermediate structure [Figure 5A]. For the purpose of comparative analysis, theoretical models were developed for both symmetric single-atomic cobalt moieties and phosphorus-free doped CoN_5S_1 sites, as illustrated in Supplementary Figure 10. By integrating the previously computed electron transfer numbers, it was determined that the ORR pathway primarily follows a 4-electron mechanism, progressing through the intermediates $*O_2$, *OOH, *O, and *OH on the optimized Co active center [Supplementary Figures 11 and 12]. Importantly, Supplementary Figure 13 revealed a pronounced stretching of the O-O bond (1.36 Å) in Co_{SA+NC}/NPSC when compared to the Co_{SA+NC}/NSC catalyst (1.06 Å), signifying an apparently enhanced activation of the O_2 molecule at the phosphorus-doped CoN_5S_1 site[39]. The free energies of the adsorbed intermediates in the ORR process and the inserted adsorption atomic structures on the Co_{SA+NC}/NPSC model were depicted in Figure 5B. Without applying additional voltage (0 V *vs.* RHE), all optimized theoretical models presented a downhill energy pathway in the ORR process, indicating their exothermic and spontaneous characteristics [Supplementary Figure 14]. At U = 1.23 V, the Co_{SA+NC}/NPSC catalyst demonstrated the lowest free energy difference (△G), effectively corroborating the findings illustrated in Supplementary Figure 13. Moreover, the third elementary step of the ORR across the Co_{SA+NC}/SC, Co_{SA+NC}/NSC, and Co_{SA+NC}/NPSC systems revealed the utmost △G, suggesting that the bottleneck reaction step (BRS) involved the transformation of *O to *OH ($*O + H^* + e^- \rightarrow *OH$) [Figure 5C]. Integrated with Co_{SA+NC}/SC (2.19 eV) and Co_{SA+NC}/NSC (1.29 eV), Co_{SA+NC}/NPSC demonstrated a notably narrow △G of the

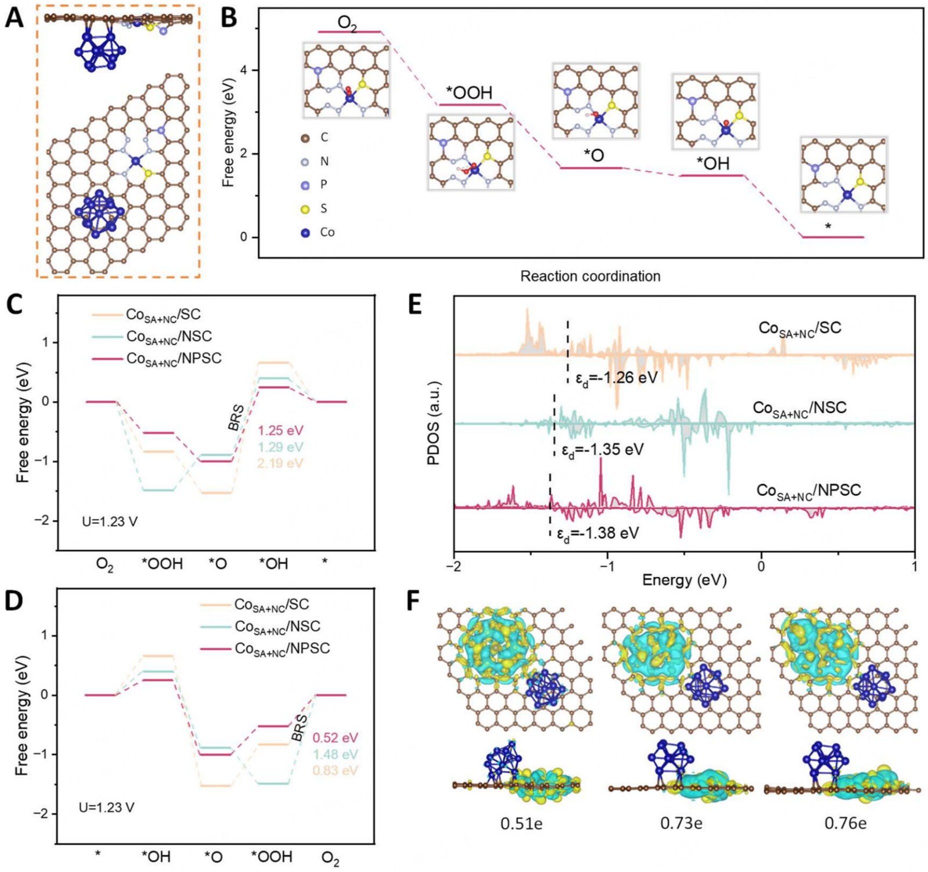

Figure 5. (A) Schematic presentation of side view and top view atomic model of Co_{SA+NC}/NPSC; (B) Pathways for the Co_{SA+NC}/NPSC at 0 V with four oxygen intermediate models inserted; (C) ORR and (D) OER free energy ladder diagrams at 1.23 V *vs.* RHE; (E) The theoretical d band center and (F) differential charge density of Co_{SA+NC}/SC, Co_{SA+NC}/NSC and Co_{SA+NC}/NPSC (yellow and cyan represented the electron accumulation and electron depletion). ORR: Oxygen reduction reaction; OER: oxygen evolution reaction; RHE: reversible hydrogen electrode.

BRS, revealing an easier *O hydrogenation occurred on Co_{SA+NC}/NPSC catalyst. These findings verified that the boosted ORR activity of Co_{SA+NC}/NPSC arose from the asymmetric coordination and incorporation of heteroatom doping, which promoted the protonation of *O and significantly improved the surface adsorption capacity for *OH at the CoN_5S_1 site. Importantly, from the perspective view of the integral ORR process, Co_{SA+NC}/NPSC showed a significantly decreased overpotential of 1.25 V than Co_{SA+NC}/SC (2.19 V) and Co_{SA+NC}/NSC (1.88 V), further underscoring its promoted efficiency in catalyzing ORR. Analogously, ΔG calculations were performed for single-atomic Co sites in the context of OER. As depicted in Figure 5D, the final step ($*OOH \rightarrow * + O_2 + H^+ + e^-$) constituted the BRS for OER at U = 1.23 V. Importantly, the ΔG values, arranged in ascending order, were Co_{SA+NC}/NPSC, Co_{SA+NC}/SC, and Co_{SA+NC}/NSC, aligning with the experimental data presented in Figure 3D. As outlined in the d-band center theory developed by Hammer and Nørskov, the relative position of the d-band center with respect to the Fermi level acted as a key "indicator" for assessing the binding affinity of single-atomic active centers toward reaction intermediates[40,41]. In Figure 5E, the ε_d value for Co_{SA+NC}/NPSC presented a downshift of 0.12 eV and 0.03 eV relative to Co_{SA+NC}/SC and Co_{SA+NC}/NSC counterparts, respectively. This suggested a more balanced binding strength between active sites and the intermediates, contributing to the promoted bifunctional ORR/OER efficiency. The electronic transmission served as a crucial descriptor of electrocatalytic performance. Consequently, the electronic characteristics of the Co_{SA+NC}/NPSC catalyst were deeply explored by charge density difference analyses. As depicted in Figure 5F, the Bader charge for Co_{SA+NC}/NPSC was determined to be 0.76 e, exceeding that of its respective counterparts. This observation suggested that the import of phosphorus atoms, along with the asymmetric coordination environment surrounding the single-atomic Co sites, facilitated enhanced electron redistribution.

CONCLUSIONS

In summary, we have developed a bifunctional oxygen electrocatalyst featuring single Co atoms integrated within an unsymmetrical Co-N_5S_1 moiety, along with NC complexes embedded in amberlite-derived N,P,S-codoped carbon frameworks, synthesized through a pyrolysis-secondary coordination approach. The deliberate design of active sites, incorporation of NCs, and heteroatom doping endowed the Co_{SA+NC}/NPSC catalyst with exceptional OER activity, outperforming benchmark IrO_2, and ORR/OER bifunctional performance in alkaline environments. The experimentally and theoretically analytical methodologies employed in this work elucidated the superior bifunctional efficiency, attributed to the optimized atomic configuration and the enhanced density-of-states distribution at the Co-N_5S_1 active centers. Additionally, the flexible ZAB assembled with Co_{SA+NC}/NPSC air cathodes demonstrated ultralong charge-discharge cycle stability, maintaining performance for over 105 h at 0 °C and 5 mA cm^{-2}. The proposed approach for the structural regulation of SA holds significant potential to advance research into other cutting-edge electrocatalytic processes, such as the hydrogen evolution reaction, nitrogen fixation, and CO_2 reduction reaction.

DECLARATIONS

Authors' contributions

Conceptualization, methodology, and writing the draft of the manuscript: Peng, J.
Contributed to the DFT theoretical calculations: Xue, T.
Graphics preparation: Li, Z.
Materials characterizations: Shi, J.
Funding acquisition, review, and editing: Wang, X.
Funding acquisition, writing-review, and editing: Xu, B.

Availability of data and materials

The data supporting their findings can be found in the Supplementary Materials.

Financial support and sponsorship

This work was supported by the Shenzhen Science and Technology Innovation Committee (Grant Nos. JCYJ20220818100406014 and KCXST20221021111616039) and SUSTech Energy Institute for Carbon Neutrality (High level of special funds, G03034K001). We also would like to acknowledge the technical support from SUSTech Core Research Facilities and the Center for Computational Science and Engineering at SUSTech.

Conflicts of interest

Wang, X. is affiliated with Shenzhen Putai Technology Co., Ltd, while the other authors have declared that they have no conflicts of interest.

Ethical approval and consent to participate

Not applicable.

Consent for publication

Not applicable.

Copyright

REFERENCES

1. Xia, Q.; Zhai, Y.; Zhao, L.; et al. Carbon-supported single-atom catalysts for advanced rechargeable metal-air batteries. *Energy. Mater.* **2022**, *2*, 200015:. DOI
2. Worku, A.; Ayele, D.; Habtu, N. Recent advances and future perspectives in engineering of bifunctional electrocatalysts for rechargeable zinc-air batteries. *Mater. Today. Adv.* **2021**, *9*, 100116. DOI
3. Ryu, J.; Park, J.; Park, J.; Kim, M. G.; Park, M. Molecular engineering of atomically dispersed Fe-N_4 and Cu-N_4 dual-sites in carbon nitride nanotubes for rechargeable zinc-air batteries. *Energy. Storage. Mater.* **2023**, *55*, 397-405. DOI
4. Liu, C.; Cui, Y.; Zhou, Y. The recent progress of single-atom catalysts on amorphous substrates for electrocatalysis. *Energy. Mater.* **2024**, *4*, 500001. DOI
5. Ji, S.; Wang, Y.; Liu, H.; et al. Regulating the electronic synergy of asymmetric atomic Fe sites with adjacent defects for boosting activity and durability toward oxygen reduction. *Adv. Funct. Mater.* **2024**, *34*, 2314621. DOI
6. Qiu, G.; Wang, J.; Qiao, H.; et al. Construction of Fe/Co-N_4 single-atom sites for the oxygen reduction reaction in zinc-air batteries. *Inorg. Chem.* **2024**, *63*, 17955-66. DOI
7. Lv, M.; Cui, C. X.; Huang, N.; et al. Precisely engineering asymmetric atomic CoN_4 by electron donating and extracting for oxygen reduction reaction. *Angew. Chem. Int. Ed.* **2024**, *63*, e202315802. DOI
8. Deng, W.; Wu, T.; Wu, Y.; et al. Microcosmic modulation of the Co-N bonding structure improves the multi-functional electrocatalytic performance. *J. Mater. Chem. A.* **2024**, *12*, 10349-58. DOI
9. Cui, T.; Wang, Y. P.; Ye, T.; et al. Engineering dual single-atom sites on 2D ultrathin N-doped carbon nanosheets attaining ultra-low-temperature zinc-air battery. *Angew. Chem. Int. Ed.* **2022**, *61*, e202115219. DOI
10. Tong, M.; Sun, F.; Xing, G.; Tian, C.; Wang, L.; Fu, H. Potential dominates structural recombination of single atom Mn sites for promoting oxygen reduction reaction. *Angew. Chem. Int. Ed.* **2023**, *62*, e202314933. DOI
11. Chen, K.; Liu, K.; An, P.; et al. Iron phthalocyanine with coordination induced electronic localization to boost oxygen reduction reaction. *Nat. Commun.* **2020**, *11*, 4173. DOI PubMed PMC
12. Chen, Z.; Niu, H.; Ding, J.; et al. Unraveling the origin of sulfur-doped Fe-N-C single-atom catalyst for enhanced oxygen reduction activity: effect of iron spin-state tuning. *Angew. Chem. Int. Ed.* **2021**, *60*, 25404-10. DOI
13. Ramaswamy, N.; Tylus, U.; Jia, Q.; Mukerjee, S. Activity descriptor identification for oxygen reduction on nonprecious electrocatalysts: linking surface science to coordination chemistry. *J. Am. Chem. Soc.* **2013**, *135*, 15443-9. DOI PubMed
14. Yasin, G.; Ali, S.; Ibraheem, S.; et al. Simultaneously engineering the synergistic-effects and coordination-environment of dual-single-atomic iron/cobalt-sites as a bifunctional oxygen electrocatalyst for rechargeable zinc-air batteries. *ACS. Catal.* **2023**, *13*, 2313-25. DOI
15. Li, M.; Zhu, H.; Yuan, Q.; et al. Proximity electronic effect of Ni/Co diatomic sites for synergistic promotion of electrocatalytic oxygen reduction and hydrogen evolution. *Adv. Funct. Mater.* **2023**, *33*, 2210867. DOI
16. Wang, Y.; Wu, J.; Tang, S.; et al. Synergistic Fe-Se atom pairs as bifunctional oxygen electrocatalysts boost low-temperature rechargeable Zn-air battery. *Angew. Chem. Int. Ed.* **2023**, *62*, e202219191. DOI
17. Wu, S.; Jiang, S.; Liu, S.; et al. Single Cu-N_4 sites enable atomic Fe clusters with high-performance oxygen reduction reactions. *Energy. Environ. Sci.* **2023**, *16*, 3576-86. DOI
18. Chen, Y.; He, T.; Liu, Q.; et al. Highly durable iron single-atom catalysts for low-temperature zinc-air batteries by electronic regulation of adjacent iron nanoclusters. *Appl. Catal. B. Environ.* **2023**, *323*, 122163. DOI
19. Zhang, J.; Wang, Q.; Qiu, C.; et al. Boosting activity of Fe-N_4 sites in single-Fe-atom catalysts via S in the second coordination sphere for direct methanol fuel cells. *Cell. Rep. Phys. Sci.* **2023**, *4*, 101330. DOI
20. Zhao, Y.; Shen, Z.; Huo, J.; et al. Epoxy-rich Fe single atom sites boost oxygen reduction electrocatalysis. *Angew. Chem. Int. Ed.* **2023**, *62*, e202308349. DOI
21. Gong, X.; Song, P.; Han, C.; Xiao, Y.; Mei, X.; Xu, W. Heterogeneous single-atom catalysts for energy process: recent progress, applications and challenges. *Energy. Mater.* **2023**, *3*, 300016. DOI
22. Li, Z.; Zhong, X.; Gao, L.; et al. Asymmetric coordination of bimetallic Fe-Co single-atom pairs toward enhanced bifunctional activity for rechargeable zinc-air batteries. *ACS. Nano.* **2024**, *18*, 13006-18. DOI
23. Yang, Y.; Li, B.; Liang, Y.; et al. Hetero-diatomic CoN_4-NiN_4 site pairs with long-range coupling as efficient bifunctional catalyst for rechargeable Zn-air batteries. *Adv. Sci.* **2024**, *11*, e2310231. DOI
24. Li, X.; Qin, J.; Lin, Q.; et al. Electron spin broken-symmetry of Fe-Co diatomic pairs to promote kinetics of bifunctional oxygen electrocatalysis for zinc-air batteries. *Adv. Sci.* **2024**, *11*, e2401187. DOI
25. Rao, P.; Deng, Y.; Fan, W.; et al. Movable type printing method to synthesize high-entropy single-atom catalysts. *Nat. Commun.* **2022**,

13, 5071. DOI PubMed PMC

26. Shang, H.; Zhou, X.; Dong, J.; et al. Engineering unsymmetrically coordinated Cu-S_1N_3 single atom sites with enhanced oxygen reduction activity. *Nat. Commun.* **2020**, *11*, 3049. DOI PubMed PMC
27. Guan, G.; Liu, Y.; Li, F.; et al. Atomic cobalt metal centers with asymmetric N/B-coordination for promoting oxygen reduction reaction. *Adv. Funct. Mater.* **2024**, *34*, 2408111. DOI
28. Zhou, Y.; Liu, Y.; Wang, Z.; et al. Fe-Co dual atomic doublets on N, P codoped carbon as active sites in the framework of heterostructured hollow fibers towards high-performance flexible Zn-air battery. *Energy. Storage. Mater.* **2023**, *59*, 102772. DOI
29. Sheng, J.; Sun, S.; Jia, G.; Zhu, S.; Li, Y. Doping effect on mesoporous carbon-supported single-site bifunctional catalyst for zinc-air batteries. *ACS. Nano.* **2022**, *16*, 15994-6002. DOI
30. Zhou, Y.; Lu, R.; Tao, X.; et al. Boosting oxygen electrocatalytic activity of Fe-N-C catalysts by phosphorus incorporation. *J. Am. Chem. Soc.* **2023**, *145*, 3647-55. DOI
31. Wang, Z.; Jin, X.; Xu, R.; et al. Cooperation between dual metal atoms and nanoclusters enhances activity and stability for oxygen reduction and evolution. *ACS. Nano.* **2023**, *17*, 8622-33. DOI
32. Wan, X.; Liu, Q.; Liu, J.; et al. Iron atom-cluster interactions increase activity and improve durability in Fe-N-C fuel cells. *Nat. Commun.* **2022**, *13*, 2963. DOI
33. Ao, X.; Zhang, W.; Li, Z.; et al. Markedly enhanced oxygen reduction activity of single-atom Fe catalysts via integration with Fe nanoclusters. *ACS. Nano.* **2019**, *13*, 11853-62. DOI
34. Yang, H. G.; Sun, C. H.; Qiao, S. Z.; et al. Anatase TiO_2 single crystals with a large percentage of reactive facets. *Nature* **2008**, *453*, 638-41. DOI
35. Perdew, J. P.; Burke, K.; Ernzerhof, M. Generalized gradient approximation made simple. *Phys. Rev. Lett.* **1996**, *77*, 3865. DOI PubMed
36. Schimka, L.; Harl, J.; Stroppa, A.; et al. Accurate surface and adsorption energies from many-body perturbation theory. *Nat. Mater.* **2010**, *9*, 741-4. DOI
37. Chadi, D. J. Special points for brillouin-zone integrations. *Phys. Rev. B.* **1976**, *13*, 5188. DOI
38. Tan, Y.; Wang, Y.; Li, A.; Zhang, Y.; Zhang, Y.; Cheng, C. Double synergetic FeCo-nanoparticles and single atoms embedded in N-doped carbon nanotube arrays as efficient bifunctional catalyst for high-performance zinc-air batteries. *Mater. Today. Energy.* **2022**, *29*, 101138. DOI
39. Wang, Z.; Lu, Z.; Ye, Q.; et al. Construction of Fe nanoclusters/nanoparticles to engineer FeN_4 sites on multichannel porous carbon fibers for boosting oxygen reduction reaction. *Adv. Funct. Mater.* **2024**, *34*, 2315150. DOI
40. Liu, S.; Li, Z.; Wang, C.; et al. Turning main-group element magnesium into a highly active electrocatalyst for oxygen reduction reaction. *Nat. Commun.* **2020**, *11*, 938. DOI PubMed PMC
41. Wang, P.; Zhang, R.; Wang, K.; et al. Simultaneously constructing asymmetrically coordinated cobalt single atoms and cobalt nanoclusters via a fresh potassium hydroxide clipping strategy toward efficient alkaline oxygen Rreduction reaction. *Energy. Mater. Adv.* **2023**, *4*, 0042. DOI